

Approaches to X-ray CT evaluation of in-situ experiments on damage evolution in an interpenetrating metal-ceramic composite with residual porosity

Joél Schukraft, Christoph Lohr, Kay André Weidenmann

Angaben zur Veröffentlichung / Publication details:

Schukraft, Joél, Christoph Lohr, and Kay André Weidenmann. 2023. "Approaches to X-ray CT evaluation of in-situ experiments on damage evolution in an interpenetrating metal-ceramic composite with residual porosity." *Applied Composite Materials* 30 (3): 815–31. <https://doi.org/10.1007/s10443-023-10115-x>.

Nutzungsbedingungen / Terms of use:

CC BY 4.0

Dieses Dokument wird unter folgenden Bedingungen zur Verfügung gestellt: / This document is made available under these conditions:

CC-BY 4.0: Creative Commons: Namensnennung

Weitere Informationen finden Sie unter: / For more information see:

<https://creativecommons.org/licenses/by/4.0/deed.de>





Approaches to X-ray CT Evaluation of In-Situ Experiments on Damage Evolution in an Interpenetrating Metal-Ceramic Composite with Residual Porosity

Joél Schukraft¹ · Christoph Lohr¹ · Kay André Weidenmann¹

Received: 20 October 2022 / Accepted: 8 February 2023 / Published online: 23 March 2023
© The Author(s) 2023

Abstract

An interpenetrating metal-ceramic composite of AlSi10Mg and an open porous alumina foam, with residual porosity is investigated for the material damage under compressive load within an X-ray CT in-situ load stage. The focus of the research is on damage detection and evaluation with the commercial Avizo[®] software by ThermoFisher Scientific. Four different approaches are used to detect the material damage and compared afterward on their efficiency in detecting the material damage volume but not the porosity within the material. Image Stack Processing combined with different filtering techniques, as well as Digital Volume Correlation is used in this work to separate the material porosity and the material damage. For the here investigated material system with mainly spherical pores, a geometrical filter was very successful to separate porosity and damage. Nevertheless, the Digital Volume Correlation based approach showed many advantages in damage detection and turned out to be the approach of choice regarding damage onset.

Keywords X-ray computed tomography (CT) · 3D visualization · Analysis of damage evolution · Digital Volume Correlation (DVC) · Interpenetrating phase composite (IPC)

1 Introduction

For composite materials, constantly increasing requirements in performance are demanded to meet the current challenges with new approaches to solutions and for progress with an economic and environmental benefit. Therefore, a better understanding of the mechanisms in the material and the damage behavior for precise engineering and (structural) component design is necessary [1]. To investigate the damage evolution in composites, different methods are in use. X-ray computed tomography (CT) based in-situ experiments became a much-chosen method in the last decade, for material investigation, as the Review of Maire and Withers [2] and the paper of Salvo et al. [3] show. Advantages of the method are the 3-dimensional visualization of cracks and the inner of the material [4]. Landis and Keane

✉ Joél Schukraft
joel.schukraft@mrm.uni-augsburg.de

¹ Institute of Materials Resource Management, Augsburg University, Am Technologiezentrum 8, 86159 Augsburg, Germany

[5] give an insight to the background and the possibilities of high flux monochromatic X-ray microtomography. Different studies on 2D and 3D crack detection have been made, and a variety of approaches arose.

Metal associated materials for crack detection, were investigated by Kastner et al. [6] who investigated the 3D microstructure of cast Al-alloys. For processing the data, they used local and global grey value thresholds, provided by VGStudio MAX 2.0. For a certain alloy (AlZn8Mg2Cu2) they used a growing algorithm for segmenting the pores. Kastner et al. [7] investigated a thermo-mechanically treated Mg-alloy with high resolution X-ray computed tomography. Phase transition, increase of porosity and crack-growth is detected under compression at temperatures between 250 and 350 °C. Data processing was carried out with VGStudio MAX 2.2.

For composites, especially fiber reinforced composites, various progresses have been made. An overview is given by the review of Garcea et al. [8]. Yu et al. [9] investigated different approaches of crack detection in a glass-fiber reinforced composite material, examined via X-ray CT. In their approaches they focus on spatial resolution, contrast, signal-to-noise ratio, full width at half maximum, user friendliness and measurement time. Scott et al. [1] investigated an carbon fiber epoxy composite and the influence of void on the damage mechanism in a multi-scale CT and the correlation to fiber break probability. For segmentation of the voids, they used a trainable segmentation tool, implemented in Fiji™. A further development of the software can be found in Arganda-Carreras et al. [10]. Gigliotti et al. [11] investigated a 3D woven carbon fiber epoxy composite with residual porosity. The damage occurring in their studies has lighter gray values than the porosity. Therefore, segmentation of the pores from the rest of the material could be carried out with the Avizo® segmentation editor. A region growing algorithm could be applied to detect the cracks semi-manual in the same software.

A ceramic-matrix-composite, investigated in literature is a SiC/SiC composite, investigated by Saucedo-Mora et al. [12]. They used an intensity threshold to segment the porosity from the material within the Avizo® software, as the contrast between the material and the pores is sufficient high. During tensile testing it was not possible to resolve damage in the microstructure with a resolution of 17,5 nether 1,75 μm . The crack detection is not described in detail. Crack location was determined by evaluating the strain field in the sample during mechanical testing via digital volume correlation (DVC). The LaVision DaVis software was used for DVC evaluation with anisotropic interrogation subsets, due to the thin wall thickness. The subset size was $128 \times 128 \times 256$ voxels. As reference, the initial unloaded specimen scan was taken. The error in displacement magnitude is stated to 8,5 μm (also compare Vertyagina et al. [13]). Polygranular graphite was investigated by Marrow et al. [14] via in-situ X-ray as well as neutron diffraction and DVC evaluation to determine the strains within the mechanically loaded sample. A phase retrieval algorithm was not used in their study to separate the porosity. The LaVision DaVis software was used for DVC evaluation with a subset size of $256 \times 256 \times 256$ voxels. The reference tomograph was recorded at a preload of 10 N.

Next to fiber reinforced composites, concrete structures stood in focus of investigation and improvement of damage detection in the last decade. As concrete structures also contain a certain amount of porosity, a selection of research results is mentioned here. Several successful approaches were made and the investigations yielded a variety of achievements. Ehrig et al. [15] tested the quality of template matching, sheet filter computed from the eigenvalues of the Hessian matrix and the perlocation algorithm for different concrete materials and compared it with a manual evaluated sample. The 3D extended sheet filter had the lowest false discovery rate, thick cracks as well as bending and branching of cracks

were detected reliably. Fujita et al. [16] describe detailed a method for crack detection in concrete structures. Pre-processing of the images, followed by a line filter and a final thresholding process lead to success in their studies. Next to these methods, intelligent and self-learning systems were included in the research in recent years. Several studies focus on the development of convolutional neural networks (cnn) for automated crack detection, as Dorafshan et al. [17], Dong et al. [18] and Tian et al. [19] for example. Especially for systematic crack pattern, breakthroughs could be achieved. But a lot of data is necessary, as well as training time and manual work [18] and control of the network: Paetsch for example, who discussed the possibilities and limitations of automatic feature extraction in 3D-CT images of concrete specimen, states, that a parameter-free out-of-the-box detection of cracks with the method he presented is not recommendable [20]. Next to the question of effort of cnn's, also the microstructure of the investigated material, as well as the damage development plays a role for the success of the approach. On the one hand, pattern in the microstructure, for example built by anisotropic structures as fiber reinforcements, as well as certain crack pattern or propagation direction support the evaluation and make specific strategies and simplifications possible. Restrictions in the evaluation on certain material system and the exclusion of more general or isotropic material systems accompany with this evaluation approaches, which makes it difficult for most of interpenetrating phase composites (IPC). In the investigation of Paetsch [20] for example, the machine learning approach requires a clear crack structure. Tian et al. [19] state, next to their achievements in segmentation limitations of the algorithm in image resolution, shape, and size. A minimal crack size of 100 μm is required for detection. Variations in image resolution and complex geometries influence the segmentation quality of the algorithm. Zou et al. [21] mention intense computation for big volumes, as e.g. the here presented volume. The problem of cracks with a gray scale in the range of one of the materials also appears here in their study, while binary thresholding is required for their segmentation process.

While the grey scale values of cracks and damage differ for most composites significantly from the image background [22], residual porosity in the material complicates the evaluation process for crack detection. For the here investigated material group of interpenetrating metal ceramic composites, no publication could be found on this topic, for the best knowledge of the authors. Previous investigations have shown, the grey scale value of cracks and porosity have the same range [23] and so automated evaluation makes it difficult to differentiate.

Therefore, this study focuses on standardized methods of CT image evaluation, with a minimal effort in computation resources and evaluation time and investigates different approaches within the commercial Avizo[®] software by ThermoFisher Scientific to compare the success and quantitative significance of each and show up the possibility of different segmentation processes on the damage evolution in an interpenetrating metal-ceramic composite with residual porosity.

2 Experimental

2.1 Material

The investigated material system, consisting of an open porous alumina foam and an AlSi10Mg light-weight aluminum alloy is fabricated via gas pressure infiltration technique. Due to its similarity in X-ray absorption, between the metallic aluminum phase and

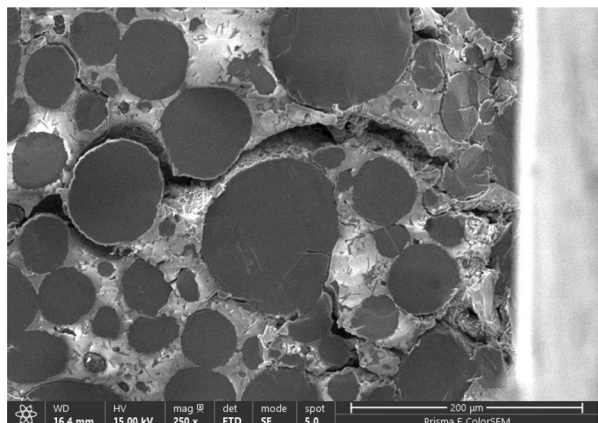
the ceramic alumina and the correlated challenge in phase differentiation, it is chosen for this investigation. The ceramic preform is manufactured by Morgan Advanced Materials Haldenwanger GmbH, Waldkraiburg, Germany, in a patented process [24]. The homogeneous porosity has a median pore radius of 10 μm and a mean pore radius of 14,4 μm , as characterized in advance [25]. The liquid metal infiltration under support of gas-pressure is schematically described by the authors in [25]. Heating up the ceramic preform in an evacuated vessel (residual pressure of maximum $2 \cdot 10^{-2}$ mbar) with AlSi10Mg slabs up to 700 °C, melts the metallic alloy so it surrounds the ceramic preform within the crucible. With a pressure of Argon gas up to 60 bar, the liquid metal is then infiltrated into the open-porous structure under hold temperature. After a dwell time of 10 min, cooling of the vessel is initiated, and the infiltrated composite could be removed from the vessel after the pressure is released at room temperature. Samples were produced, by cutting sample slices of approximately 5 mm thickness out of the infiltrated sample block with a cutting machine “Servocut® 301 - MA” by Metkon, Bursa, Turkey. With a diamond hollow drill, manufactured by Günther Diamantwerkzeuge, Idar-Oberstein, Germany and the dimensions of 3 mm as an outer diameter, the cylindrical samples were cut out of the sample slices. The microstructure with the ceramic and metallic phase, residual porosity and superficial damage under compression is presented in the SEM image in Fig. 1.

The investigation of this composite is relevant to improve the application field of light weight metals. Higher stiffness, strength and wear resistance could already be achieved for metal matrix composites in propeller shafts, engine blocks, brakes, piston rings or connecting rods, e.g. Interpenetrating phase composites outperform these properties [26], promising higher hardness and additionally have an adjustable coefficient of thermal expansion which is relevant at elevated temperatures at 200 °C and above. Previous studies on the mechanical characterization of the composite material can be found elsewhere [23, 25, 27].

2.2 In-situ X-ray CT Scanning

The data was obtained using a Phoenix Nanotom 180 m tomograph, GE Sensing & Inspection Technologies GmbH, Wunstorf, Germany, equipped with a diamond target. By damaging specimens inside the computed tomograph with a specially designed in-situ load stage, different damage states could directly be investigated, holding the sample under load and therefore the developed cracks open. The 3 mm diameter sample is hold on one of the

Fig. 1 SEM image of the composite material with residual porosity and compression damage after failure, close to the compression stamp (right in the image). The load axis is horizontal in the image. The metallic phase has a dark gray appearance, including metallic precipitations, the ceramic phase is light gray/white and residual porosity as well as damage black. Cracks grow in the ceramic phase, the interface and the metallic phase. A scale bar and beam parameters are given in the image



alumina compression stamps with molten rosin. The second compression stamp is brought onto the sample with a preload of 40 N, after the in-situ stage is mounted. The load faces are only fixed by friction and allow shearing of the sample, as the results show. The influence of the rosin is negligible. The setup is shown in Fig. 2 and a detailed description of the load stage can be found in Thum et al. [28].

To investigate different damage states the specimen was loaded to a certain extent, followed by a CT measurement of the loaded sample. The compressive testing was then continued until reaching the next load step. Compression testing was chosen, to generate stable damage in form of cracks, which are opened during the investigation of each load step. In this study, two pre-scans were taken, before loading the sample (scan 01 and scan 02), and the scans of four different load steps are analyzed (load step 1: 235 MPa, load step 2 before the stress maximum: 370 MPa, load step 3: 360 MPa, load step 4: 290 MPa, each after the stress maximum). The beam source was operated at 80 kV and 180 μ A and the integration time was set at 2000 ms, averaging five images for each of the 2000 positions/ 360° . With a focus-object distance (FOD) of 13.8 mm and a focus-detector distance (FDD) of 600 mm, the resulting CT data had a voxel size of $(2,3 \mu\text{m})^3$. Before starting the CT measurement, an observation area (ROI) was defined in the sample free scanning field for background corrections. Additionally, the Shift Correction and Auto Scan Optimizer provided in the acquisition software Phoenix data sx2 (GE Sensing & Inspection Technologies GmbH, Wunstorf, Germany) were activated. To reconstruct a 3D image from the CT data, the corresponding Phoenix data sx2 reconstruction software was used, setting the beam hardening correction factor to 8.6 and applying the provided ScanOptimizer and reconstruction filters. Avizo[®] software by ThermoFisher Scientific, Waltham, USA was used for 3D image evaluation of the scanned data and is described in the following subchapter.

2.3 3D Image Evaluation Approaches

The hardware of the computer, used for this study is an Intel(R) Xeon(R) W-2145 CPU with 3,70 GHz and 8 cores. The RAM has 256 GB and a GPU by NVIDIA of type Quadro P5000 16 GB and 288 GB/s bandwidth. The evaluation was carried out in Avizo[®], by ThermoFisher Scientific, Waltham, USA. System requirements depend on the size of the processed data and the workflow. Regarding ThermoFisher Scientific [29], the CPU performance increases

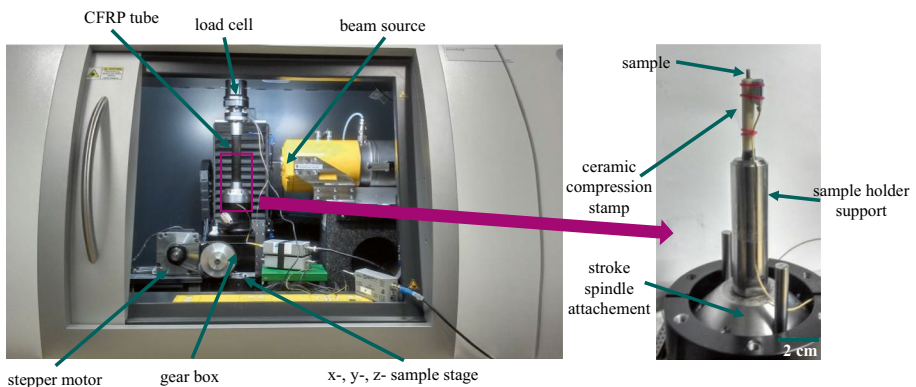


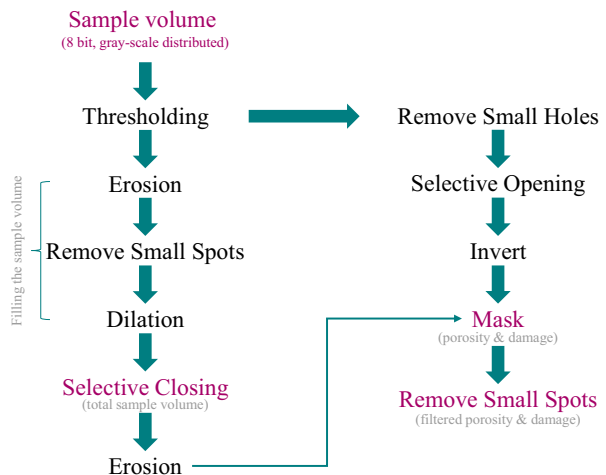
Fig. 2 In-situ X-ray CT set-up (left) with magnification of the sample, fixed with rosin on the compression stamp (right)

almost linear up to 8 cores. Minimum requirements are 1 GB GPU, 6 to 8 times of the data size for RAM and solid state drives are recommended for fast transfer rates [29].

Special commands and operations within the software will be given in italic letters in the following. For equal grayscale distribution in all scans, the *normalize grayscale* module was applied on every scan and gray values were distributed between 0 and 255 (8 bit). Then a sub-volume of the scan was extracted, which contained the relevant sample volume.

Different approaches were made to investigate the quality and the quantitative reliability of each crack detection method regarding the influence of the residual porosity in the material. All relevant data (pre-load step scans as well as the scans at every load step) were rearranged with the function *register images* in an *iso-scale transformation* with *metric correlation* and the *quasi-newton optimizer* to compensate a possible shift of the sample between the scans. In the new and for all regions of interest (ROI) identical position, the scans were *resampled* and *interpolated* with a Lanczos algorithm [30]. For approaches A, B and C (described below), an *image stack process (ISP)* was used, which works slice-wise for optimized and automated processing and reduces computation time. The image stack was processed slice-wise, perpendicular to the load direction. The whole ISP consists of 11 steps, as given in Fig. 3. With the first 6 steps (on the left side), the material sample was freed from beam artifacts and measuring setup, to receive the relevant sample volume only: A *thresholding* process, followed by five volume manipulating operations were carried out. The *erosion* step, followed by the *remove small spots* step, removed small artifacts around the sample volume. A *dilation* step, to compensate the eroded volume and increase it over the original volume, combined with a *selective closing* were used to delete inner vacancies within the sample volume. A final *erosion* step reduced the original sample size volume about some voxels to avoid surface artifacts occurring in the porosity detection. To detect the damage and porosity of the sample within this sample volume, the *thresholded* data from above were taken for the following 5 steps (compare right side of Fig. 3): Artifacts were removed with a *remove small holes* and *selective opening* step and the volume was inverted after. With a *mask* step, the received data are masked with the before prepared sample volume, to detect damage and porosity inside the sample volume only and to remove all artifacts around the sample. Details, changed in the process for approach D *digital volume*

Fig. 3 Overview of the Image Stack Processing (ISP) in Avizo with 6 steps to extract the sample volume (compare left side) and 5 steps to detect the inner porosity and damage of the sample (compare right side). Input and output data are colored in purple letters



correlation (DVC), are described in the respective paragraph. The output data of the ISP for each approach, is a defined volume of the isolated sample without any surroundings as artifacts on the one hand and the volume of the inner low gray values of the sample, representing the residual porosity and damage or a filtered variant, depending on the approach, on the other hand.

- (A) In the first approach, the porosity of the sample was determined within the *ISP* for the unloaded sample, where no damage to the compression test did occur. For all the further images, with the applied load on the sample, the porosity volume of the first image was subtracted from the detected residual porosity and damage with the *arithmetic* function. By subtracting the porosity of the material, only damage-induced porosity should remain in the sample.
- (B) The second approach was to filter the porosity and the damage regarding geometrical characteristics. Residual porosity in the material occurs often in a different shape compared to the damage. For this material, the residual porosity has mainly spherical shape and the damage of cracks a narrow and two-dimensional extended geometry. The resulting data from the *ISP* were labeled in a 3D interpretation and then filtered with the function *filter by measure*. The chosen filter criterion *sphericity* was applied for different thresholds in the 3D voxel-based images. The perfectly and almost round objects, with a sphericity of close to 1 were filtered away as “porosity”, where objects with smaller sphericity values and a higher surface to volume ratio (values from 0 up to the threshold) were kept as damage. The thresholds were set to 0,5; 0,7; 0,8; 0,9 and 0,94 to study the influence of the threshold on the results. Comparisons for validation were made in the preloaded sample scans, where no damage by compression occurred.
- (C) A third approach was to filter the size of the residual porosity during *ISP* with an additional final step of the function *remove small spots* and to investigate the influence of filtered size on the damage volume ratio. The value was increased until the porosity of the unloaded sample was not detected anymore, similar to approach B, and the influence of the total detected porosity was evaluated. Finally, the value was set to 50 pixels for all scanned images.
- (D) For the fourth approach the *DVC* [31, 32] of Avizo[®] was used. As described above, all data were *registered* and the ROIs *resampled*. To process the data uniformly, a bounding box, with the coordinate origin always at the same corner was set to all investigated data. Regarding Hild [33], different coarse to fine meshes were created and tested on the geometry. The *radial autocorrelation* module [34] was used to investigate the correlation length of the microstructure and the *DVC accuracy* function applied to control the precision of the correlation for each mesh size. A global, finite-element-based approach [35] was chosen to carry out *DVC* for each load step and to determine the displacement field in comparison to the undeformed reference volume. Finally, a mesh size of 350 μm was considered to be purposeful and the carried out *DVC* calculation converged within 500 iteration cycles, successfully. As a reference of the undeformed sample and to control the quality of the scans and the correctly chosen parameter for calculation, the two pre-scans were compared in the *DVC* module and their displacement and strain investigated. As an output file of the *DVC*, a residuals file is calculated, comparing the conformity of both scans and showing local discontinuities, as they appear from damage in the material volume. Further output files of the *DVC*, less relevant in this study, are the displacement and strain files and the mesh. The residuals file is in a special way of interest for this damage approach, as it contains extreme values

(black and white) where damage occurs in the material, whilst the deformed or still undeformed areas appear in a uniform scalar field of noisy grayscales [35]. Therefore, these values are used in the fourth approach, to determine sample damage within the sample. An *ISP*, analog to the first three approaches, is used to separate the discontinuities and display them three-dimensionally in the sample ROI. The threshold was set regarding the noisy grayscale as described below and a *remove small spots* operation with a maximum of 20 pixels was used, before the results were set as output.

3 Results

For evaluation and comparison of the different approaches, the damage volume of each approach is given relative to the respective ROI volume at each load step. As reference, in Fig. 4 a diagram of the ROI volume at each load step is given, as well as the overall volume content of porosity and damage, from the ISP without any filtering or selection. As Fig. 4 shows, the volume of the ROI increases over the load steps, as well as the sum of the volume of porosity and damage.

In the following, the results of the before presented four approaches for damage evaluation are compared regarding sensitivity of the method, quantitative reliability and the influence due to the porosity on the detected damage content. A direct comparison of all approaches with the total “porosity and damage” (compare Fig. 4) and the “corrected porosity and damage” is given in Fig. 5. As scan 01 and scan 02 are captured from the undeformed sample, there should be no damage in the sample yet. Therefore, the “corrected porosity and damage” is the quantitative value of detected pore volume in scan 01, subtracted from scan 02 and all the other load steps to give a quantitative comparison of the increase in damage content. Figure 5 shows the increase in detected damage with each approach for the best fitted method. Closer details to each approach will be given in the following.

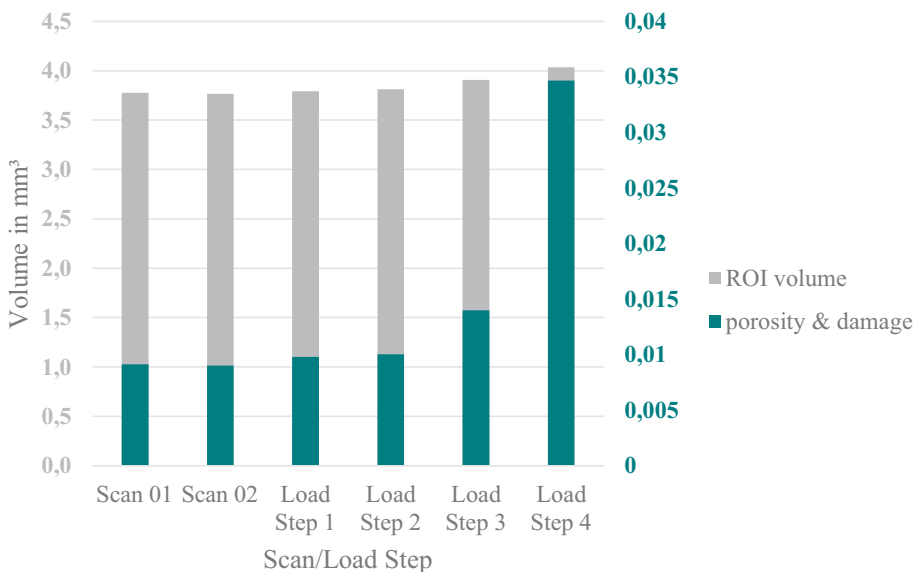


Fig. 4 Volume evaluation of the investigated ROI over the load steps and volume content of porosity and damage

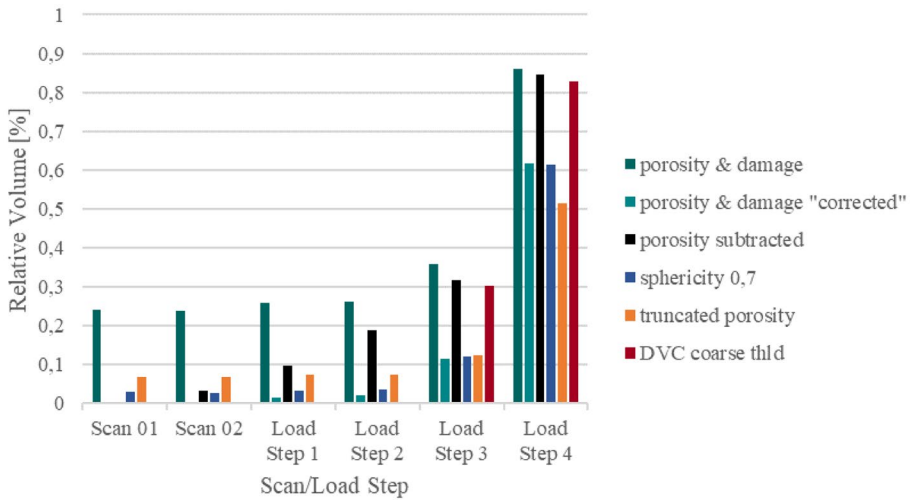


Fig. 5 Overview of the quantitative evaluation of the whole sample section for approaches A – D, as well as the total detected “porosity and damage”, and the correction with the “porosity in scan 01” subtracted from the “sum of porosity & damage“ of each other load step, given as “porosity & damage “corrected””. For approach B and D, only the best fitting parameter set is given

Like shown in Fig. 6A, approach A gives very low relative volume content of damage for the second scan. An increase of damage is visible for each following load step. The increase reaches almost the volume of the sum of damage and porosity for load step 4.

Different thresholds for approach B are given in Fig. 6B. For comparison, the sum of damage and porosity is plotted in a corrected way also in the graph. Therefore, the value of scan 01 – as it only should content porosity and no damage – is subtracted from every other scan and load step result to free the value from porosity and show damage only. As Fig. 6B shows, according to the chosen threshold, the given damage value varies in a wide range. For the preloaded images, scan 01 and scan 02, the graph shows that an elimination of detected damage is only possible for a sphericity threshold of 0,5. For the following load steps the sphericity threshold of 0,5 lies under the value of the corrected sum of porosity and damage graph. A sphericity threshold of 0,8 and higher results in higher values than the corrected damage graph and detects a high portion of “damage” for scan 01 and scan 02. For a chosen sphericity threshold of 0,7 a small amount of damage is detected for scan 01 and scan 02. For the development over the four load steps the values follow the graph of the corrected sum of porosity and damage graph and show a good agreement.

Approach C shows a detected damage volume, following the course of the sum of damage and porosity. With a value of the double compared with approach B and a sphericity threshold of 0,7, the detected damage for the undeformed sample is quite high and lies above the corrected sum of porosity and damage. For higher loads, the value decreases relatively to the sum of porosity and damage value, as Fig. 6C shows.

Approach D is given for a coarse and fine thresholding. The noisy grayscale results of the DVC are gaussian distributed. Nevertheless, the question arises, where to set the threshold correctly for a correct visualization of damage. The “fine” thresholding therefore is set near the full width at half maximum of the gaussian bell. The “coarse” thresholding on the other hand is set with a small distance, outside of the gaussian bell, to detect absolute extrema only. As the diagram in Fig. 6D shows, the choice of the

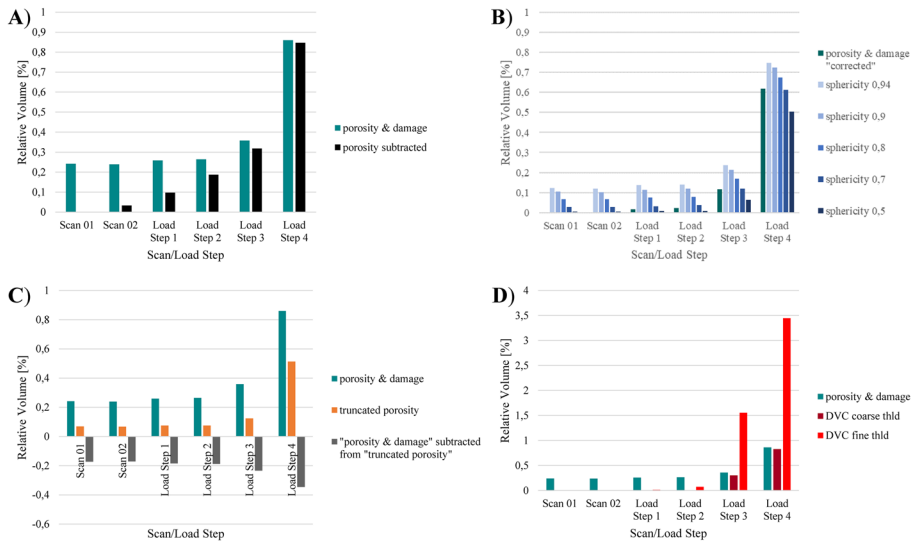


Fig. 6 Overview of the quantitative results of the different approaches. **Top left:** Results of detected damage in **approach A**, compared with the “sum of porosity & damage”. **Top right:** Results of detected damage in **approach B**, compared with the corrected porosity & damage (“porosity in scan 01” subtracted from the “sum of porosity & damage” is given as “porosity & damage “corrected””). **Bottom left:** Results of detected damage in **approach C**, compared with the “sum of porosity & damage” and the calculated difference between both values. **Bottom right:** Results of **approach D**, compared with the “sum of porosity & damage”

threshold position has a big influence on the detected damage volume. For the DVC comparison of scan 01 and scan 02, both thresholds for this approach doesn’t show a remarkable proportion of damage until load step 2. The fine thresholding then increases strongly and overgoes the sum of porosity and damage with a factor of 4 for load step 3 and load step 4. The coarse thresholding is also increasing but stays beyond the sum of porosity and damage but reaches it almost for load step 4. In comparison to the corrected sum of porosity and damage, the coarse thresholding value of approach D lies 1/3 above it for load step 4 (compare values in Figs. 5 and 7).

To consider the local dissolution of the pores next to the quantitative determination, 2D sections of load step 4 are compared in Fig. 7. Exemplary, the sphericity approach is shown for several filtering thresholds to be discussed in detail.

Figure 7 shows the gray-scale distributed image of the composite, where the lighter grey structures represent the alumina and the slightly darker grey represent the aluminum alloy (in 2D the aluminum phase builds round structures). The white spots within the metallic phase represent the precipitations of the aluminum alloy, containing heavy elements as iron e.g. The dark grey values close to black represent the inner, residual porosity of the material, due to closed porosity in the ceramic foam and infiltration faults during gas pressure infiltration (compare Horny et al. [25]). The damage in the sample ranges over a wide range of grey scale values. As given in the green box in the upper row, the damage can be detected by the evaluation method. The darker the gray scale in the crack is, the better it can be detected. Cracks close to the resolution limit are visible by eye but not detectable by the ISP anymore. On the right side in the green box, the approach of the truncated porosity is given, to get a visual impression of the filtering and falsifying of the microstructural damage.

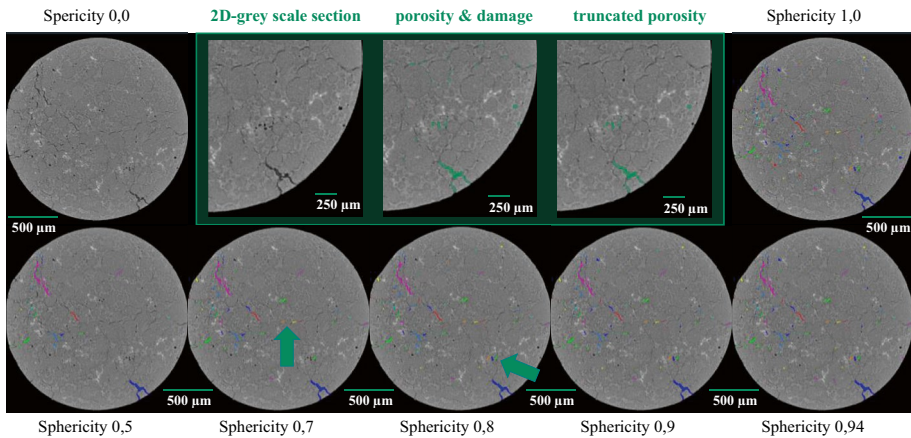


Fig. 7 Representative transverse 2D slices of the specimen cylinder, perpendicular to the load direction of the CT-sample at load step 4. In the upper row, in the green box, sections of higher magnification are given for the CT raw data (left), the detected porosity and damage, as described above (center) and the truncated porosity (right). Around the box, the values of the sphericity approach are varied exemplary for all approaches. Arrows mark relevant differences in comparison to the next lower value

Next to this, the sphericity filtering threshold is given for all the presented values (0,0 and 1,0 are added to get a reference of the unlabeled and total labeled damage and porosity). From sphericity 0,0 to sphericity 1,0 the stepwise increase of detected cracks is visible. The green arrow in the sphericity 0,7 image highlights the added smaller cracks in comparison to sphericity 0,5. In the next step, for sphericity 0,8 the addition of a bigger amount of porosity with the increase of the value is highlighted with the respective arrow. For a further increase of the value, more of the spherical shaped pores are included within the threshold and added to the porosity, as seen in the figure for sphericity 0,9, sphericity 0,94 sphericity 1,0 (no filtering).

For comparison of the visual results and local dissolution of cracks in 3D of each approach, Fig. 8 shows the detected damage for the load steps 2 and 4 as well as the unloaded sample scan 02 in comparison.

4 Discussion

As the results have shown, the different approaches are sensitive to several influences and the quantitative result differs for each method (compare for instance Fig. 5).

Figure 3 shows, the absolute volume increase of the investigated ROI is decades larger than the detected sum of the volume of porosity and damage. During compression testing, the porosity ratio increases the volume of the ROI, because the ROI height is restricted geometrically while the diameter is limited by the sample surface only. For load steps 3 and 4 also the incipient shearing of the sample increases the volume within the ROI additionally. It becomes obvious that the absolute damage increase is only a fraction of the volume increase and the main part is given by the transverse expansion of the compression. In relative terms, however, the increase in porosity and damage is up to 280% way bigger than the relative volume increase of 6,8%. This justifies the consideration of relative damage volume of each approach regarding the respective ROI volume and includes the additional

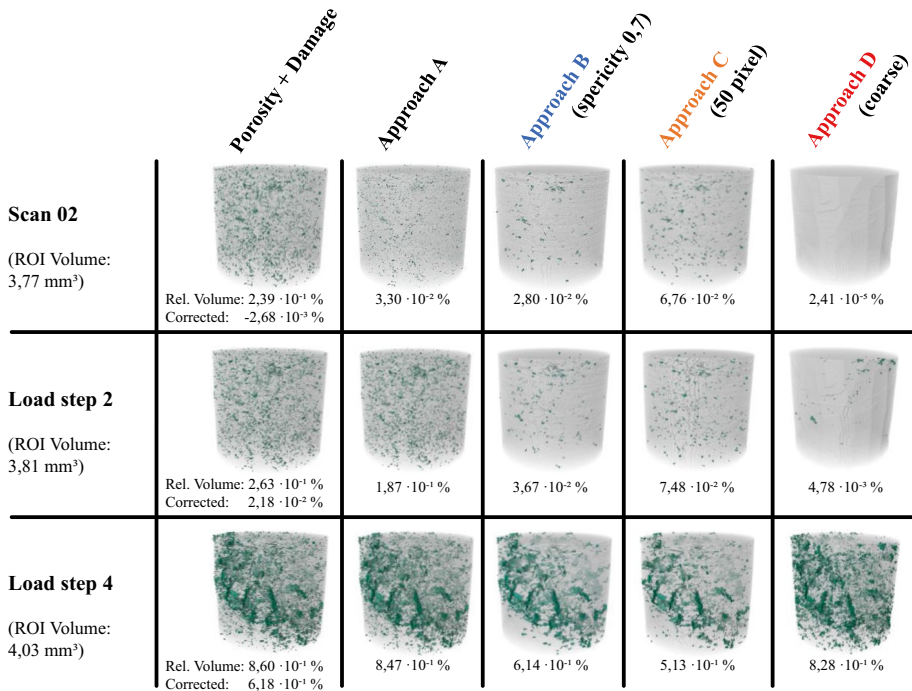


Fig. 8 Overview of the visual damage detection with the different investigated approaches of the unloaded sample (scan 02), 370 MPa (load step 2) and 290 MPa (load step 4) of the whole 3D ROI with transparent volume (gray). Additional information about the ROI volume, as well as the detected relative damage volume of each approach are given (A: subtraction of initial porosity, B: geometrical filtering, C: “cut off” porosity and D: DVC detection of discontinuities). For comparison the detection of the sum of porosity and damage are given, including corrected numbers, where the initial porosity of scan 01 is subtracted from every other value

porosity and damage, appearing for high loads in the ROI, which have been outside of it before loading the sample.

In the following the quantitative aspects as well as the local dissolution of damage should be discussed, in order of the approaches.

Approach A is a precise method for small deformations. A good result could be achieved for the values of scan 02 and the load step 1. The differences to zero for the second scan, as well as the fine dispersed and very small detected damage, visible in Fig. 8, can be explained by the partial volume effect, leading to local differences in the grey value and the resulting local changes in the detection of the ISP (cf. Fig. 8, scan 02 for approach A). For increasing deformation, the deviation of the method and the inefficiency in the separation of porosity and arising damage can be explained by the shift of the porosity due to deformation of the sample (compare for load step 4, Fig. 7 right side in the green box and the values of the relative volume for approach A in Fig. 8). With increasing deformation, an increase of detected damage and also increasing proportion of porosity detected as damage can be recognized, which finally reaches the sum of the detected damage and porosity in the ROI (compare Figs. 5 and 6A). This shows that for big deformation almost all pores changed the position of their main volume regarding the first scan.

Approach B is strongly dependent on the filtering threshold. In literature also in other scientific contexts, this approach is used as a simple and robust technique, like given for example by Ouzounis et al. [36] for medical technology or by Du Plessis et al. [37] for additive manufacturing monitoring of unmolten particles in laser sintering. To eliminate the detection of porosity as damage in the unloaded scans, a sphericity threshold of 0,5 or less is required. For the following load steps the sphericity threshold of 0,5 underestimates the damage in the ROI, as the comparison with the corrected sum of porosity and damage shows (compare Fig. 6B). This can partly be explained by the detection of the damage with the ISP, where thin cracks cannot be detected as a related object, caused by the resolution limit of the scan (see Fig. 7). Therefore small, limited, and spherical objects appear instead of 2D expanded cracks before the crack size overwhelms the resolution limit of the CT scan and can be detected correctly by the ISP. A sphericity threshold of 0,8 and higher, overestimates the damage over the whole range and includes also for scan 01 and scan 02 a relevant portion of porosity, which distorts the value (see Fig. 6B). This can be justified in the range of sphericity, the main part of the porosity in the investigated material lies in. The higher the threshold is set, the higher is the portion of porosity detected as damage over the whole investigation range. A chosen sphericity threshold of 0,7 also includes a small amount of porosity for the first scans but matches very well for the further damage evolution with the corrected graph of the sum of damage and porosity. Next to the quantitative point of view, the 2D section of the microstructure shows (highlighted with the green arrows in Fig. 7 for sphericity 0,7 and 0,8), the sphericity threshold of 0,7 contains the relevant amount of damage but only includes a minor fraction of porosity. This makes it an adequate candidate for detection of damage with this method for the differentiation of pores and damage in the case of different geometrical appearance, for materials where microdamage is beneficial in increasing ductility and energy absorption. As the comparison of the 3D depicted ROIs show, the detected porosity in the unloaded scans is restricted to the bigger, infiltration caused pores, which extend sickle-shaped in the phase boundary between the ceramic struts and the metal-filled pores of the ceramic foam.

Approach C cuts off the damage from a certain size on and loses all information about damage beyond that filtering threshold. In comparison to approach B, an increase in porosity due to mechanical loading can be recognized, because the grown pore exceeded the threshold then. For approach B, a growing, spherical-shaped pore would be filtered off for all damage stages, nevertheless, an increase in size due to damage would occur. As Fig. 6C shows, approach C cuts off a markable amount of damage in progressive damage stages, but still includes porosity in the detected damage, as the undeformed value in scan 01 and scan 02, as well as the 2D section of load step 4 on the right side in the green box in Fig. 7 shows. Analogous to approach B, the values can be shifted, related to the chosen threshold. As the curve of approach C shows an overestimation of the damage in the early stage, a higher cut-off threshold would be necessary. But as it underestimates the damage volume here, as the “difference between “sum of porosity and damage” and approach C” shows in Fig. 6C, a decrease in the cut-off threshold would be necessary. Therefore, the method is only for qualitative description and quantitative tendencies of damage permissible and not suitable for absolute quantitative crack evaluation or local dissolution of the total damage.

Approach D shows for the coarse thresholding as well as the fine a value almost zero for the unloaded sample. The low numbers for the first load step correlate with the microstructural investigations of the sample and fit best, in comparison to the other approaches. This precise determination of damage can be explained by the DVC based evaluation method [35], which differs significantly from the other approaches and relies on the comparison of the gray values and shifted pattern between the load levels. In literature, Saucedo-Mora

et al. [12] used the DVC method for damage detection in composites. They detected the location of damage, but no quantitative evaluation was carried out. In the discussion of the filtering of growing porosity due to mechanical load, the DVC method is sensitive for this phenomenon, because a difference to the before scanned load step occurs. It therefore has an advantage over approach B and C. Also, in the visual detection of the damage (see Fig. 8), a difference in localization between the approaches can be found and show the difference in the underlying method, as well as the influence of falsely detected porosity in the damage volume of the other approaches. For the progressive damage steps, the damage value in this approach also increases and reaches unrealistic high values for the fine thresholding. Reasons can be the local loss of correlation, as the local displacement gets in the range of the correlation length (see Madi et al. [34]). Compared with approach B with a sphericity threshold of 0,7 (see Fig. 5), the values of the graph as well as the local dissolution of damage in Fig. 8, show a higher deviation from the corrected sum of damage and porosity.

Compared to the in literature presented methods given in the introduction, for the interpenetrating metal ceramic composite, the here presented investigation methods work with a manageable time effort, hard- and software equipment and give good results for the cracks in approach B, differing in their geometry from the spherical shaped porosity.

5 Summary and Conclusion

The evaluation of damage in the investigated IMCC material with the commercial Avizo[®] software by ThermoFisher Scientific has shown the possibility of successful quantitative evaluation of damage content in a material system with residual porosity. In comparison of all approaches within this study, the necessity became obvious, to deal intensively with the unfiltered data, occurring damage phenomena and the resolution limit of these, in order to avoid excluding individual damage phenomena by filtering and thus systematically falsifying the result. The chosen approaches show different sensitivity and accuracy for damage and porosity separation. A big advantage of all approaches is the robust detection for cracks, independent of the damage stage. The limiting factor lies in the quality of the raw data alone and depends on the resolution, which determines the lower limit of crack visibility.

- To subtract the initial porosity of the sample from every following scan, turned out not to be promising. On the one hand, displacement of the porosity leads to a high amount of porosity detected as damage. On the other hand, partial volume effects influence the porosity detection and lead to false identified pore outlines.
- To cut off the phenomena, in the range of the porosity and smaller can lead to strong filtering of damage phenomena and loss of information, dependent on the ratio of the pore size and the damage. Nevertheless, this approach might be promising for other materials with a specific and known range of porosity outside the range of damage.
- For the investigated IMCC material with a mainly spherical-shaped porosity, the geometrical approach with a sphericity threshold of 0,7 achieved the best results for the entire damage area, even if a small amount of residual porosity remains ($6,7 \cdot 10^{-2}\%$) at the beginning of the damage (compare Figs. 5 and 7).
- In this area, the DVC approach is more meaningful due to its underlying method of absolute initial porosity exclusion. It can indicate the onset of damage more specifically and detect it more reliably. For the quantitative investigation of damage, it must be considered, if the effort of DVC can outweigh the higher precision in comparison to the fast and simple evaluation path of the sphericity threshold.

Acknowledgements We want to thank Morgan Advanced Materials Haldenwanger GmbH for the friendly supply of complimentary preform material.

Funding Open Access funding enabled and organized by Projekt DEAL. The financial support of the German Research Foundation (DFG) within the project WE 4273/17-1 is gratefully acknowledged.

Data Availability The raw/processed data required to reproduce these findings cannot be shared at this time as the data also forms part of an ongoing study.

Declarations

Conflict of Interest The authors declare that they have no known competing financial interests or personal relationships that could have appeared to influence the work reported in this paper.

Open Access This article is licensed under a Creative Commons Attribution 4.0 International License, which permits use, sharing, adaptation, distribution and reproduction in any medium or format, as long as you give appropriate credit to the original author(s) and the source, provide a link to the Creative Commons licence, and indicate if changes were made. The images or other third party material in this article are included in the article's Creative Commons licence, unless indicated otherwise in a credit line to the material. If material is not included in the article's Creative Commons licence and your intended use is not permitted by statutory regulation or exceeds the permitted use, you will need to obtain permission directly from the copyright holder. To view a copy of this licence, visit <http://creativecommons.org/licenses/by/4.0/>.

References

1. Scott, A.E., Sinclair, I., Spearing, S.M., Mavrogordato, M.N., Hepples, W.: Influence of voids on damage mechanisms in carbon/epoxy composites determined via high resolution computed tomography. *Compos. Sci. Technol.* **90**, 147–153 (2014). <https://doi.org/10.1016/j.compscitech.2013.11.004>
2. Maire, E., Withers, P.J.: Quantitative X-ray tomography. *Int. Mater. Rev.* **59**, 1–43 (2014). <https://doi.org/10.1179/1743280413Y.0000000023>
3. Salvo, L., Suéry, M., Marmottant, A., Limodin, N., Bernard, D.: 3D imaging in material science: Application of X-ray tomography. *C. R. Phys.* **11**, 641–649 (2010). <https://doi.org/10.1016/j.crhy.2010.12.003>
4. Beckmann, F., Grupp, R., Haibel, A., Huppmann, M., Nöthe, M., Pyzalla, A., Reimers, W., Schreyer, A., Zettler, R.: In-situ synchrotron X-ray microtomography studies of microstructure and damage evolution in engineering materials. *Adv. Eng. Mater.* **9**, 939–950 (2007). <https://doi.org/10.1002/adem.200700254>
5. Landis, E.N., Keane, D.T.: X-ray microtomography. *Mater. Charact.* **61**, 1305–1316 (2010). <https://doi.org/10.1016/j.matchar.2010.09.012>
6. Kastner, J., Plank, B., Salaberger, D.: High resolution X-ray computed tomography of fibre- and particle-filled polymers. 18th World Conference on Nondestructive Testing (2012)
7. Kastner, J., Zaunschirm, S., Baumgartner, S., Requena, G., Pinto, H., Garcés, G.: 3D-microstructure characterization of thermomechanically treated Mg alloys by high resolution X-ray computed tomography, vol. 11, pp. 1–9. 11th European Conference on Non-Destructive Testing (2014)
8. Garcea, S.C., Wang, Y., Withers, P.J.: X-ray computed tomography of polymer composites. *Compos. Sci. Technol.* **156**, 305–319 (2018). <https://doi.org/10.1016/j.compscitech.2017.10.023>
9. Yu, B., Bradley, R.S., Soutis, C., Withers, P.J.: A comparison of different approaches for imaging cracks in composites by X-ray microtomography. *Philos. Trans. A. Math. Phys. Eng. Sci.* **374**, 20160037 (2016). <https://doi.org/10.1098/rsta.2016.0037>
10. Arganda-Carreras, I., Kaynig, V., Rueden, C., Eliceiri, K.W., Schindelin, J., Cardona, A., Sebastian Seung, H.: Trainable Weka segmentation: a machine learning tool for microscopy pixel classification. *Bioinformatics.* **33**, 2424–2426 (2017). <https://doi.org/10.1093/bioinformatics/btx180>
11. Gigliotti, M., Pannier, Y., Gonzalez, R.A., Lafarie-Frenot, M.C., Lomov, S.V.: X-ray micro-computed tomography characterization of cracks induced by thermal cycling in non-crimp 3D orthogonal woven composite materials with porosity. *Compos. A. Appl. Sci. Manuf.* **112**, 100–110 (2018). <https://doi.org/10.1016/j.compositesa.2018.05.020>

12. Saucedo-Mora, L., Lowe, T., Zhao, S., Lee, P.D., Mummery, P.M., Marrow, T.J.: In situ observation of mechanical damage within a SiC-SiC ceramic matrix composite. *J. Nucl. Mater.* **481**, 13–23 (2016). <https://doi.org/10.1016/j.jnucmat.2016.09.007>
13. Vertyagina, Y., Mostafavi, M., Reinhard, C., Atwood, R., Marrow, T.J.: In situ quantitative three-dimensional characterisation of sub-indentation cracking in polycrystalline alumina. *J. Eur. Ceram. Soc.* **34**, 3127–3132 (2014). <https://doi.org/10.1016/j.jeurceramsoc.2014.04.002>
14. Marrow, T.J., Liu, D., Barhli, S.M., Saucedo Mora, L., Vertyagina, Y., Collins, D.M., Reinhard, C., Kabra, S., Flewitt, P.E.J., Smith, D.J.: In situ measurement of the strains within a mechanically loaded polygranular graphite. *Carbon*. **96**, 285–302 (2016). <https://doi.org/10.1016/j.carbon.2015.09.058>
15. Ehrig, K., Goebbels, J., Meinel, D., Paetsch, O., Prohaska, S., Zobel, V.: Comparison of crack detection methods for analyzing damage processes in concrete with computed tomography. *International Symposium on Digital Industrial Radiology and Computed Tomography* (2011)
16. Fujita, Y., Mitani, Y., Hamamoto, Y.: A method for crack detection on a concrete structure. In: 18th International Conference on Pattern Recognition (ICPR'06), pp. 901–904. IEEE (2006)
17. Dorafshan, S., Thomas, R.J., Maguire, M.: Comparison of deep convolutional neural networks and edge detectors for image-based crack detection in concrete. *Constr. Build. Mater.* **186**, 1031–1045 (2018)
18. Dong, Y., Su, C., Qiao, P., Sun, L.: Microstructural crack segmentation of three-dimensional concrete images based on deep convolutional neural networks. *Constr. Build. Mater.* **253**, 119185 (2020). <https://doi.org/10.1016/j.conbuildmat.2020.119185>
19. Tian, W., Cheng, X., Liu, Q., Yu, C., Gao, F., Chi, Y.: Meso-structure segmentation of concrete CT image based on mask and regional convolution neural network. *Mater. Des.* **208**, 109919 (2021). <https://doi.org/10.1016/j.matdes.2021.109919>
20. Paetsch, O.: Possibilities and limitations of automatic feature extraction shown by the example of crack detection in 3D-CT images of concrete specimen. In: 9th conference on industrial computed tomography, pp. 1–9. iCT (2019)
21. Zou, Y., Yao, G., Wang, J.: Research on 3D crack segmentation of CT images of oil rock core. *PLoS One*. **16**, e0258463 (2021). <https://doi.org/10.1371/journal.pone.0258463>
22. Paetsch, O., Baum, D., Ehrig, K., Meinel, D., Prohaska, S.: Automated 3D crack detection for analyzing damage processes in concrete with computed tomography. *iCT Conference, Wels* (2012)
23. Schukraft, J., Lohr, C., Weidenmann, K.A.: 2D and 3D in-situ mechanical testing of an interpenetrating metal ceramic composite consisting of a slurry-based ceramic foam and AlSi10Mg. *Compos. Struct.* **263**, 113742 (2021). <https://doi.org/10.1016/j.compstruct.2021.113742>
24. Lavrentyeva, O.: Verfahren zur Herstellung von aufgeschäumten keramischen Werkstoffen sowie dadurch herstellbarer keramischer Schaum (2015). (DE(DE102015202277A))
25. Horny, D., Schukraft, J., Weidenmann, K.A., Schulz, K.: Numerical and experimental characterization of elastic properties of a novel, highly homogeneous interpenetrating metal ceramic composite. *Adv. Eng. Mater.* (2020). <https://doi.org/10.1002/adem.201901556>
26. Mattern, A., Huchler, B., Staudenecker, D., Oberacker, R., Nagel, A., Hoffmann, M.J.: Preparation of interpenetrating ceramic-metal composites. *J. Eur. Ceram. Soc.* **24**, 3399–3408 (2004). <https://doi.org/10.1016/j.jeurceramsoc.2003.10.030>
27. Schukraft, J., Lohr, C., Weidenmann, K.A.: Mechanical characterization of an interpenetrating metal-matrix composite based on highly homogeneous ceramic foams. In: Hausmann, J.M., Siebert, M., von Hehl, A., Weidenmann, K.A. (eds.) *Hybrid 2020 Materials and Structures*, pp. 33–39. Sankt Augustin (2020)
28. Thum, F., Potstada, P., Sause, M.G.R.: Development of a 25kN in situ load stage combining X-ray computed tomography and acoustic emission measurement. *KEM.* **809**, 563–568 (2019). <https://doi.org/10.4028/www.scientific.net/KEM.809.563>
29. ThermoFisher Scientific: User's guide Avizo software. <https://assets.thermofisher.com/TFS-Assets/MSD/Product-Guides/users-guide-avizo-software-2019.pdf> (2019). Accessed 1 Mar 2023
30. Lanczos, C.: An Iteration Method for the Solution of the Eigenvalue Problem of Linear Differential and Integral Operators. *J. Res. Natl. Bur. Stand.* **45**, 255–282 (1950)
31. Buljac, A., Jaijin, C., Mendoza, A., Neggers, J., Taillandier-Thomas, T., Bouterf, A., Smaniotto, B., Hild, F., Roux, S.: Digital volume correlation: review of progress and challenges. *Exp. Mech.* **58**, 661–708 (2018). <https://doi.org/10.1007/s11340-018-0390-7>
32. Hild, F., Bouterf, A., Chamoin, L., Leclerc, H., Mathieu, F., Neggers, J., Pled, F., Tomičević, Z., Roux, S.: Toward 4D mechanical correlation. *Adv. Model. Simul. Eng. Sci.* **3**, 17 (2016). <https://doi.org/10.1186/s40323-016-0070-z>
33. Hild, F.: Generate a DVC mesh of complex shapes. <https://xtras.amira-avizo.com/xtras/tutorial-generate-a-dvc-mesh-of-complex-shapes> (2019). Accessed 29 Jun 2021

34. Madi, K., Gailliègue, S., Boussuge, M., Forest, S., Gaubil, M., Boller, E., Buffière, J.-Y.: Multiscale creep characterization and modeling of a zirconia-rich fused-cast refractory. *Phil. Mag.* **93**, 2701–2728 (2013). <https://doi.org/10.1080/14786435.2013.785655>
35. Madi, K., Tozzi, G., Zhang, Q.H., Tong, J., Cossey, A., Au, A., Hollis, D., Hild, F.: Computation of full-field displacements in a scaffold implant using digital volume correlation and finite element analysis. *Med. Eng. Phys.* **35**, 1298–1312 (2013). <https://doi.org/10.1016/j.medengphy.2013.02.001>
36. Ouzounis, G.K., Giannakopoulos, S., Simopoulos, C.E., Wilkinson, M.H.F.: Robust extraction of urinary stones from CT data using attribute filters. In: 16th IEEE International Conference on Image Processing (ICIP), 2009: 7 - 10 Nov. 2009, Cairo, Egypt ; proceedings. IEEE, Piscataway, NJ (2009)
37. Du Plessis, A., Yadroitsev, I., Yadroitsava, I., Le Roux, S.G.: X-ray microcomputed tomography in additive manufacturing: a review of the current technology and applications. *3D. Print. Addit. Manuf.* **5**, 227–247 (2018). <https://doi.org/10.1089/3dp.2018.0060>

Publisher's Note Springer Nature remains neutral with regard to jurisdictional claims in published maps and institutional affiliations.